Simulation Modelling Practice and Theory 100 (2020) 102039

Contents lists available at ScienceDirect

Simulation Modelling Practice and Theory

journal homepage: www.elsevier.com/locate/simpat

Analysis of flat-end milling forces considering chip formation process in high-speed cutting of Ti6Al4V titanium alloy

Mehmet Aydın[a,*], Uğur Köklü[b]

[a] Department of Industrial Product Design, Bilecik Şeyh Edebali University, Bilecik 11230, Turkey
[b] Department of Mechanical Engineering, Karamanoğlu Mehmetbey University, Karaman 70100, Turkey

ARTICLE INFO

Keywords:
Flat-end milling forces
FE modeling
High-speed orthogonal cutting
Mechanics of metal cutting
Segmented chip
Ti6Al4V alloy

ABSTRACT

This paper proposes a unified numerical and analytical approach to predict flat-end milling forces considering the chip morphology and cutting force in high-speed cutting of titanium alloy (Ti6Al4V). A two-dimensional finite element (FE) model of the orthogonal cutting process is developed by applying a displacement-based ductile failure criterion. With this FE model, the segmented chip formation is analyzed. The mesh dimension is investigated as an effective factor in the chip segmentation. The numerical results demonstrate that the chip morphology is significantly affected from the mesh dimension while the average cutting force varies slightly with the mesh dimension. The mesh dependency of the chip morphology can be decreased by applying the non-local progressive damage model involving the intrinsic material length. An attempt is also made for modeling and prediction of cutting forces in high-speed flat-end milling. The milling force constants which are generally derived from experimental calibrations are required to predict the milling forces by using the unified mechanics of cutting approach. Here, the numerical FE simulations are carried out to characterize the milling force constants. The milling forces predicted analytically are validated by comparing with those obtained from the experimental study. Finally, the behavior of the milling forces can be effectively analyzed through the proposed approach based on the chip formation process.

1. Introduction

The high-speed cutting process of titanium alloys draws the interests of many researchers, which enable a perfect surface finish and dimensional precision for industrial applications. However, it is extremely difficult to machine titanium alloys due to their high chemical reactivity and low thermal conductivity [1]. To enhance productivity and tool-life in machining titanium alloys, it is required to analyze the segmented chip formation. It can be conducted a systematic study of the segmented chip formation based on a FE model.

The mesh dependency is a major issue when establishing a FE model. This issue should be also considered in modeling the cutting process. Bäker et al. [2] analyzed the influences of different mesh densities by establishing a two-dimensional FE model of the orthogonal cutting of Ti6Al4V alloy. Their results demonstrated that the segmented chips were very similar geometrically, and the finer mesh caused a lower cutting force. Hortig and Svendsen [3] presented a more comprehensive investigation of the influences of the mesh dimension and orientation on the chip formation during high-speed cutting of Inconel 718. It was found from their study that a smaller mesh dimension caused an increase in the chip segmentation frequency but a decrease in the cutting force. Zhang et al.

---

[*] Corresponding author.
E-mail address: mehmet.aydin@bilecik.edu.tr (M. Aydın).

https://doi.org/10.1016/j.simpat.2019.102039
Received 1 July 2019; Received in revised form 3 December 2019; Accepted 8 December 2019

Nomenclature

a_p	cutting depth
A	initial yield strength (MPa)
b	cutting width
B	hardening modulus (MPa)
C	strain rate sensitivity
d	pitch of two neighbor shearing planes
$\mathrm{d}F_t$, $\mathrm{d}F_r$, $\mathrm{d}F_a$	differential tangential, radial and axial milling forces
D	damage parameter
$D_1 \ldots D_5$	JC failure model parameters
f_{hz}	segmentation frequency
f_t	feed per tooth
F_t, F_r	tangential and radial forces in orthogonal cutting
F_x, F_y, F_z	milling forces in X, Y and Z directions
t_{min}	valley height of segmented chip
t_{max}	peak height of segmented chip
i	helix or obliquity angle
K_{te}, K_{re}, K_{ae}	tangential, radial and axial edge force constants
K_{ts}, K_{rs}, K_{as}	tangential, radial and axial shear force constants
L	characteristic length
m	thermal softening coefficient
n	strain-hardening coefficient
P	hydrostatic pressure (MPa)
r	chip thickness ratio in orthogonal cutting
S_r	segment ratio
t	undeformed chip thickness in orthogonal cutting
t_{nj}	instantaneous chip thickness in milling
T_m	melting temperature of workpiece material (1630 °C)
T_w	workpiece temperature
T_0	room temperature (25 °C)
$\bar{u}^p$	equivalent plastic displacement
$\bar{u}_f^p$	failure plastic displacement
V	cutting speed
V_c	chip sliding velocity
α_r, α_n	radial and normal rake angles
β	friction angle at rake face
γ	flank angle
$\Delta\bar{\varepsilon}^p$	equivalent plastic strain increment
$\bar{\varepsilon}^p$,$\dot{\bar{\varepsilon}}^p$	equivalent plastic strain and strain rate
$\dot{\varepsilon}_0^p$	reference strain rate (1 s^{-1})
$\bar{\varepsilon}_{0i}$	equivalent plastic strain at the onset of damage
$\bar{\sigma}_{JC}$	equivalent stress (MPa)
η_c	chip velocity angle
τ_s	shear stress
ϕ	shear angle
ϕ_n, β_n	normal shear and friction angles
ω	damage initiation parameter

[4] suggested a two-dimensional FE model to simulate the orthogonal cutting of Ti6Al4V alloy and produced a segmented chip. They compared the cutting forces obtained from different mesh dimensions with a measurement result, and a strong mesh dependency was observed. Shams and Mashayekhi [5] also performed the numerical FE simulations with non-local damage model to analyze the mesh dependency of chip morphology and cutting force when machining aluminum alloy (A2024-T351). The literature review shows that a systematic investigation of the mesh dimension has not been comprehensively carried out to overcome the mesh dependency in cutting simulation.

A constitutive material model is required to define the material behavior during the numerical investigation of cutting process with the aid of the FE analysis. The most common material model applied in the cutting analysis was presented by Johnson and Cook (JC) [6], and this model was employed in many cutting process simulations [7–10]. Besides, metal cutting processes can be analyzed more realistically by including a progressive damage model into the FE models. The most significant stage in the progressive damage model is to accurately implement the failure criterion. Ambati and Yuan [11] analyzed the mesh dependency using the progressive damage model with plastic displacement for cutting simulations. They showed that the mesh dimension could slightly affect the computational results when the failure criterion was dependent on a characteristic length. Chen et al. [12] established a FE model based on the JC failure model with an energy-based failure criterion for high-speed cutting of Ti6Al4V alloy. They modified the failure parameter for a cutting condition. Then, the same failure parameter was implemented to different cutting conditions.

Due to the advancement of machine tools and cutting tools, the high-speed milling has become a cost-effective manufacturing process. A reliable prediction of cutting forces before milling operations is essential for high productivity and quality. Two types of analytical models are used commonly for predicting milling forces: exponential and linear edge force models. In exponential force model, shearing and ploughing mechanisms are modeled by a single force constant. In linear edge force model, milling forces are predicted from shear and edge force constants. In general, two basic approaches are used for the identification of milling force constants: unified mechanics of cutting and mechanistic approaches. In the first approach presented by Budak et al. [13], milling force constants were established from the orthogonal cutting parameters. Similarly, Rao and Shunmugam [14] suggested an analytical force model for micro end milling and determined the milling force constants using the oblique cutting principles. Wan et al. [15] presented an approach for establishing the milling force constants through a few milling operations rather than orthogonal cutting operations. The mechanistic approach relies on average cutting forces measured in one rotation of milling tool, where milling force constants are empirically established by the least squares method. Dikshit et al. [16] studied the dependence of milling force constants on rotational speeds using the mechanistic approach for ball-end milling. They found that these empirical constants varied with the variation in rotational speed. Aydın et al. [17] modeled milling forces through a mechanistic approach based on the force distribution of the cutting part of end mill. Their calibration approaches include a practical mechanism for extrapolating the milling force constants.

In recent studies, milling force constants have been extracted using FE-based techniques. Adetoro and Wen [18] carried out FE analyses based on the Arbitrary Lagrangian-Eulerian (ALE) formulation, which includes the advantages of Lagrangian and Eulerian algorithms, to determine mechanistically the milling force constants. Gonzalo et al. [19] also presented an approach to obtain the milling force constants through orthogonal and oblique cutting processes. In this approach, the constants were identified by using mechanistic and numerical FE models. Aydın and Köklü [20] established two different FE models with the ALE method using Langrangian and Eulerian-Lagrangian boundaries to identify the milling force constants. They used the milling force constants to model cutting forces in ball-end milling. Experimental studies on the determination of milling forces have been conducted by many researchers, but only a few accurate numerical studies involving the prediction of milling forces based on the FE modeling can be found in the literature. In these numerical studies, the milling force constants were identified by analyzing the continuous chip formation at conventional cutting speeds. There are not any studies which contribute to the prediction of milling force constants by modeling the segmented chip formation under high cutting speed conditions.

This paper proposes a unified numerical and analytical approach to predict flat-end milling forces by performing the numerical simulations of orthogonal cutting of Ti6Al4V alloy at high cutting speed. Firstly, a simplified FE model of two-dimensional orthogonal cutting is developed, which uses a progressive damage model with a displacement-based ductile failure criterion. Using this FE model, segmented chips are produced. The mesh dimension is studied as an effective factor in the segmented chip formation, and a systematic study is presented to decrease the mesh dependency. Latter contribution of this study is to model the flat-end milling forces by using the advantage of the short calculation time of the unified mechanics of cutting approach and replacing the experimental study by numerical FE simulation to extract the milling force constants.

2. Fe modeling procedure

2.1. Modeling data and geometrical model

The FE analysis software Abaqus/Explicit was employed to provide a deep insight into the segmented chip formation in high-speed cutting of Ti6Al4V alloy. The simplest cutting process is one in which the cutting edge is normal to the vector of cutting speed. This is called the orthogonal cutting. A two-dimensional fully thermo-mechanically orthogonal cutting model was developed as illustrated in Fig. 1. It was established in accordance with undeformed chip thickness (t) for different cutting conditions. All geometrical dimensions vary with undeformed chip thickness.

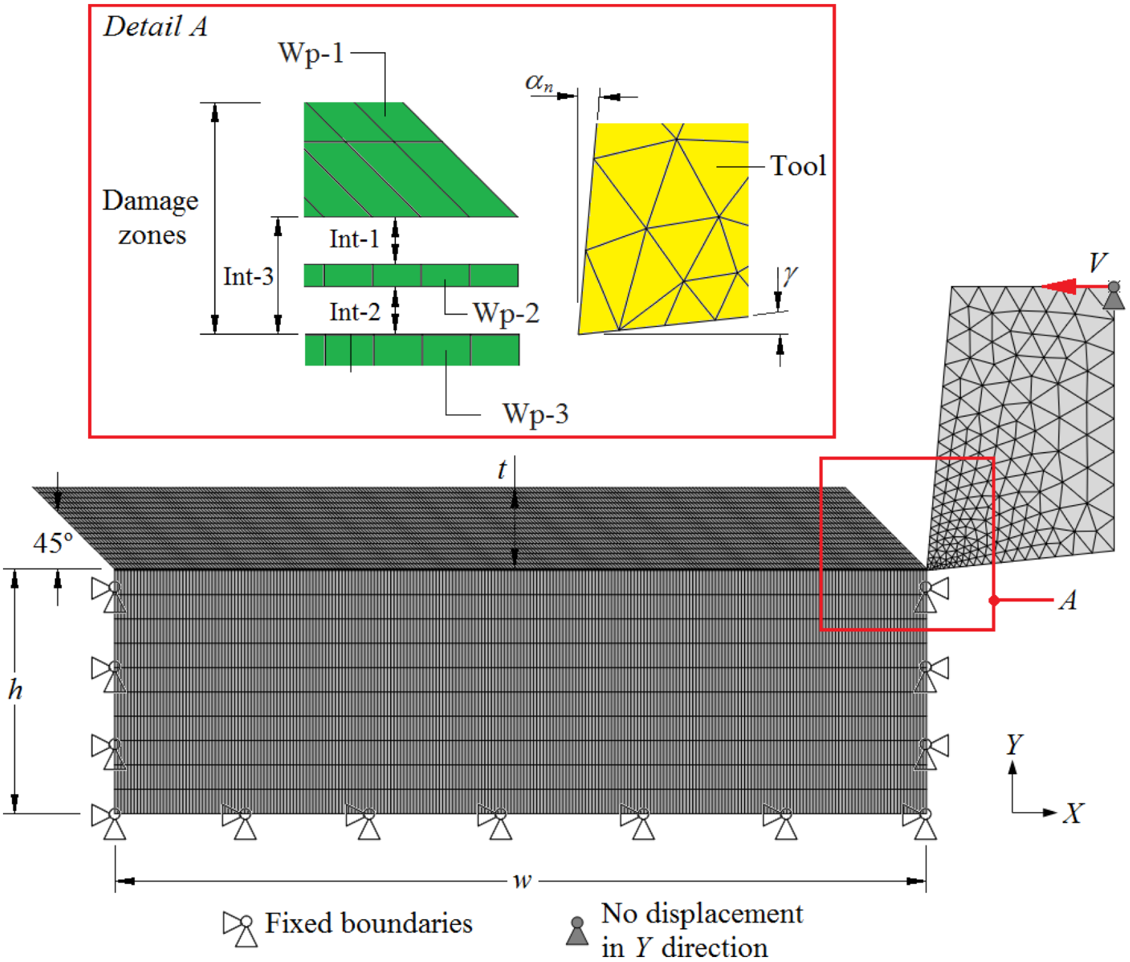

Fig. 1. Two-dimensional orthogonal cutting model.

The workpiece was consisted of three geometrical parts: (1) the chip part (Wp-1), (2) the separation layer (Wp-2) and (3) the workpiece support (Wp-3). A chamfer was also established on the chip part to prevent distortion problems at the beginning of analysis, as shown in Ref. [21]. The ratio of h to t was 3 while the ratio of w to t was 10. The ratios of these geometrical dimensions were kept constant at different undeformed chip thicknesses. The thickness of separation layer was one fiftieth of the undeformed chip thickness, which was adjusted to a very small size for modeling the chip formation. The contact pairs Int-1 and Int-2 were defined for the interfaces between the different parts of the workpiece, which were established through rough friction formulation and penalty contact algorithm. Their normal behaviors were set as "hard" contact, and a separation was not allowed after contact. An excessively large value was implemented to define the thermal conductance between the contact pairs. Thus, these three parts can be regard as one body when the heat transfer is considered. The contact pair Int-3 between the chip part and workpiece support was also assigned to avoid their penetration to each other.

A 4-node quadrilateral element (CPE4RT) was utilized to mesh the deformable workpiece, and enhanced hourglass control was applied for the chip elements. The cutting tool was modeled as a rigid body with a sharp edge and meshed by using a 3-node triangle element (CPE3T). For boundary conditions, the workpiece support was fixed from its lower, back and front surfaces, and the cutting tool was allowed to move horizontally from the right to the left but constrained vertically. Initially, the cutting tool and workpiece were kept at room temperature. The contact between the cutting tool and the chip part was described with the kinematic contact algorithm, where the tool was the master surface and the lower and front sides of the chip were the slave surface. Since the friction at tool–chip interface was not properly known, it was neglected in the simulations in this study, based on Refs. [22, 23].

The cutting tool was tungsten carbide insert whose the normal rake (α_n) and flank (γ) angles were 5° and 6°, respectively. The cutting speed (V) was 300 m/min, which was given to the cutting tool. The undeformed chip thickness (t) was varied from 0.1 to 0.3 mm with the increase of 0.05 mm, which corresponds to the feed in the orthogonal cutting. The cutting width (b) was taken as 2 mm.

2.2. Material model and properties

The workpiece material was Ti6Al4V alloy and modeled by the JC constitutive material model [6], which provides a satisfactory representation of the workpiece material behavior in high-speed cutting. This model is given in Eq. (1).

$$\bar{\sigma}_{JC} = [A + B\,(\bar{\varepsilon}^{p})^{n}]\left[1 + C\ \text{In}\left(\frac{\dot{\bar{\varepsilon}}^{p}}{\dot{\bar{\varepsilon}}_0^{p}}\right)\right]\left[1 - \left(\frac{T_w - T_0}{T_m - T_0}\right)^{m}\right] \tag{1}$$

The JC constitutive model parameters of Ti6Al4V are listed in Table 1 whereas the physical and mechanical properties of the workpiece and cutting tool are presented in Table 2.

2.3. Chip formation criterion

A two-stage progressive damage model [25] was applied to simulate the chip formation during high-speed cutting of Ti6Al4V alloy, i.e., damage initiation and damage evolution. In this model, the displacement-based ductile failure criterion with linear softening was dependent on a characteristic element length (L) to mitigate the mesh dependency.

2.3.1. Damage initiation

The JC failure model [26] was applied as an initial damage criterion, which is formulated by Eq (2). It contains five failure parameters D_i (i = 1, 2, 3, 4, 5), which represent initial failure strain, exponential factor, triaxiality factor, strain rate factor and temperature factor, respectively. The JC failure model parameters of Ti6Al4V are given in Table 3.

$$\bar{\varepsilon}_{0i} = \left[D_1 + D_2 \exp\left(D_3 \frac{P}{\bar{\sigma}_{JC}}\right)\right]\left[1 + D_4\ \text{In}\left(\frac{\dot{\bar{\varepsilon}}^{p}}{\dot{\bar{\varepsilon}}_0^{p}}\right)\right]\left[1 + D_5\left(\frac{T_w - T_0}{T_m - T_0}\right)\right] \tag{2}$$

The damage in an element is allowed to initiate when a scalar damage parameter (ω) equals to 1. This parameter relies on the following cumulative damage law:

$$\omega = \sum\left(\frac{\Delta\bar{\varepsilon}^{p}}{\bar{\varepsilon}_{0i}}\right) \tag{3}$$

where $\Delta\bar{\varepsilon}^{p}$ is the increase of equivalent plastic strain.

2.3.2. Damage evolution

A displacement-based ductile failure criterion was adopted to manage the damage evolution during high-speed cutting of

Table 1
The JC model parameters of Ti6Al4V [24].

A (MPa)	B (MPa)	n	C	m
862	331	0.34	0.012	0.8

Table 2
The properties of workpiece and cutting tool [4, 20].

Property	Workpiece (Ti6Al4V)	Tool (tungsten carbide)
Density (kg/m^3)	4430	14,500
Poisson's ratio	0.33	0.227
Young's modulus (GPa)	110	540
Thermal conductivity (W/m °C)	6.6	84 (20 °C) 63 (1000 °C)
Specific heat (J/kg °C)	670	220
Thermal expansion (1/°C)	9×10^{-6}	5.8×10^{-6}

Table 3
The JC failure model parameters of Ti6Al4V [24].

D_1	D_2	D_3	D_4	D_5
−0.09	0.25	−0.5	0.014	3.87

Ti6Al4V, and the linear damage evolution with the plastic displacement was given by Eq. (4).

$$\bar{u}^p = L\bar{\varepsilon}^p \tag{4}$$

Where L is the characteristic element length which is defined as the square root of the element area. It is used to decrease the effect of mesh dimension. Thus, the plastic strain of shear band becomes inversely proportional to the mesh dimension. Accordingly, the equivalent plastic displacement ($\bar{u}^p$) is less affected from the mesh dimension.

The damage parameter (D) can be defined using Eq. (5).

$$D = \frac{L\,\bar{\varepsilon}^p}{\bar{u}_f^p} = \frac{\bar{u}^p}{\bar{u}_f^p} \tag{5}$$

It should be noted that when the equivalent plastic displacement ($\bar{u}^p$)reaches to the failure plastic displacement ($\bar{u}_f^p$), the parameter D in the nodes of the chip element is equal to the degradation value of 1. This chip element is completely damaged and removed from the mesh when $D = 1$. The elements which are not completely damaged also occur the chip. Meanwhile, the elements of the separation layer are deleted to separate the chip from the workpiece.

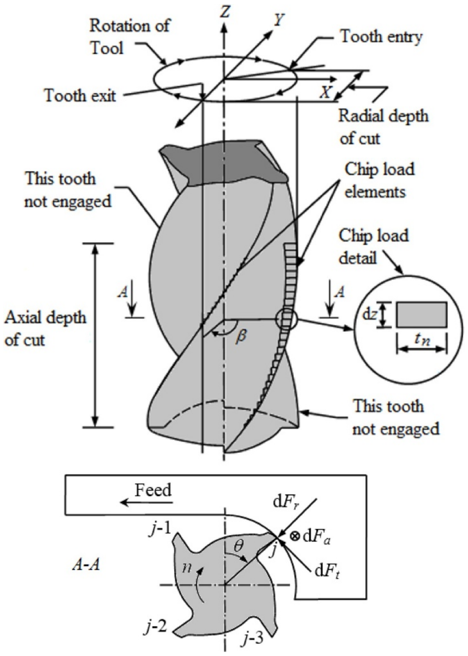

Fig. 2. Modeling of the flat-end milling [27].

3. Modeling of end milling forces

3.1. Cutting force model

A typical flat-end milling process and differential cutting forces are illustrated in Fig. 2. For modeling cutting forces, the helical teeth are uniformly discretized into a number of differential oblique segments with a height of dz.

The differential tangential (dF_{tj}), radial (dF_{rj}) and axial (dF_{aj}) cutting forces for a segment of the jth tooth consist of two mechanisms, namely shearing and ploughing, and are modeled by the following linear force model [13].

$$\begin{cases} \mathrm{d}F_{tj}(\theta, z) = [K_{te} + K_{ts}\ t_{nj}(\theta, z)]\ \mathrm{d}z \\ \mathrm{d}F_{rj}(\theta, z) = [K_{re} + K_{rs}\ t_{nj}(\theta, z)]\ \mathrm{d}z \\ \mathrm{d}F_{aj}(\theta, z) = [K_{ae} + K_{as}\ t_{nj}(\theta, z)]\ \mathrm{d}z \end{cases} \tag{6}$$

Where K_{te}, K_{re}, and K_{ae} are the tangential, radial and axial edge force constants, respectively, K_{ts}, K_{rs}, and K_{as} are the corresponding shear force constants.

The instantaneous chip thickness can be expressed by Eq. (7).

$$t_{nj}(\theta, z) = f_t \sin\beta_{ij}(z) \tag{7}$$

Where $\beta_{ij}(z) = \theta + j\theta_p - \frac{\tan i}{R} z$ is the angular position of the ith differential segment of the jth tooth at position z, f_t is the feed per tooth, θ is the rotation angle, $\theta_p = 2\pi/N$ is the pitch angle. R and N is the tool radius and tooth number, respectively.

The differential cutting forces dF_{tj}, dF_{rj} and dF_{aj} can be resolved into the X, Y and Z directions as given by Eq. (8).

$$\begin{Bmatrix} \mathrm{d}F_{xj}(\beta_{ij}(z)) \\ \mathrm{d}F_{yj}(\beta_{ij}(z)) \\ \mathrm{d}F_{zj}(\beta_{ij}(z)) \end{Bmatrix} = \begin{bmatrix} -\cos\beta_{ij}(z) & -\sin\beta_{ij}(z) & 0 \\ \sin\beta_{ij}(z) & -\cos\beta_{ij}(z) & 0 \\ 0 & 0 & 1 \end{bmatrix} \begin{Bmatrix} \mathrm{d}F_{tj} \\ \mathrm{d}F_{rj} \\ \mathrm{d}F_{aj} \end{Bmatrix} \tag{8}$$

Combining Eqs. (6) and (8) and substituting chip thickness (t_{nj}) from Eq. (7), the linear edge force model can be presented in the integral form by Eq. (9).

$$\begin{aligned} F_{xj}(\beta_{ij}(z)) &= \int_{z_{j1}}^{z_{j2}} \{\tfrac{f_t}{2}[-K_{ts}\sin 2\beta_{ij}(z) - K_{rs}(1 - \cos 2\beta_{ij}(z))] \\ &\quad + [-K_{te}\cos\beta_{ij}(z) - K_{re}\sin\beta_{ij}(z)]\}\,\mathrm{d}z \\ F_{yj}(\beta_{ij}(z)) &= \int_{z_{j1}}^{z_{j2}} \{\tfrac{f_t}{2}[K_{ts}(1 - \cos 2\beta_{ij}(z)) - K_{rs}\sin 2\beta_{ij}(z)] \\ &\quad + [K_{te}\sin\beta_{ij}(z) - K_{re}\cos\beta_{ij}(z)]\}\,\mathrm{d}z \\ F_{zj}(\beta_{ij}(z)) &= \int_{z_{j1}}^{z_{j2}} \{[K_{ae} + K_{as} f_t \sin\beta_{ij}(z)]\}\,\mathrm{d}z \end{aligned} \tag{9}$$

Where z_{j1} and z_{j2} are the axial limits of the engaged part of the jth tooth. The total X, Y and Z cutting forces at angular position $\beta_{ij}(z)$ can be determined by Eq. (10).

$$\begin{bmatrix} F_x(\beta_{ij}(z)) \\ F_y(\beta_{ij}(z)) \\ F_z(\beta_{ij}(z)) \end{bmatrix} = \sum_{j=1}^{N} \begin{bmatrix} F_{xj} \\ F_{yj} \\ F_{zj} \end{bmatrix} \tag{10}$$

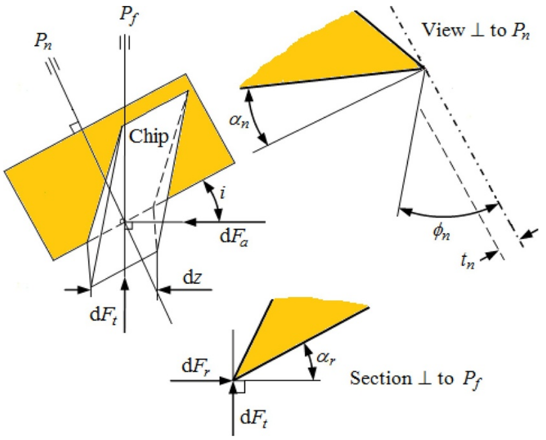

Fig. 3. Oblique cutting process for an element of a helical tooth [13].

3.2. *Extrapolation of milling force constants*

A simulation of milling forces requires the extrapolation of milling force constants, namely edge and shear force constants. To extract the edge force constants K_{te} and K_{re}, the tangential (F_t) and radial (F_r) forces are numerically found through a set of orthogonal cutting simulations at different undeformed chip thicknesses (t) but constant width of cut (b) and cutting speed (V). These force components are split into two parts, namely edge forces (F_{te}, F_{re}) and shear forces (F_{ts}, F_{rs}), as described by Eq. (11). The constants K_{te} and K_{re} are identified from the edge forces per unit width of cut (b) of the force-undeformed thickness functions. The K_{ae} is generally assumed as zero [28].

$$F_t = \underbrace{K_{te}\, b}_{F_{te}} + \underbrace{K_{ts}\, b\, t}_{F_{ts}}, \quad F_r = \underbrace{K_{re}\, b}_{F_{re}} + \underbrace{K_{rs}\, b\, t}_{F_{rs}} \tag{11}$$

The cutting action of a helical tooth in milling is treated as oblique cutting with the inclination angle equal to the helix angle (i) and the normal rake angle (α_n) which is dependent on the radial rake angle (α_r) and helix angle (i), as given in Eq. (12) [13].

$$\tan\alpha_n = \tan\alpha_r \cos i \tag{12}$$

The shear force constants K_{ts}, K_{rs} and K_{as} are derived from the force equilibrium of oblique cutting model [13] in Fig. 3, which are given by Eq. (13).

$$\begin{aligned}
K_{ts} &= \tau_s\left(\frac{\cos(\beta_n-\alpha_n) + \tan\eta_c \sin\beta_n \tan i}{\sin\varphi_n \sqrt{\cos^2(\varphi_n+\beta_n-\alpha_n)+\tan^2\eta_c \sin^2\beta_n}}\right)\\
K_{rs} &= \tau_s\left(\frac{\sin(\beta_n-\alpha_n)}{\sin\varphi_n \cos i \sqrt{\cos^2(\varphi_n+\beta_n-\alpha_n)+\tan^2\eta_c \sin^2\beta_n}}\right)\\
K_{as} &= \tau_s\left(\frac{\cos(\beta_n-\alpha_n)\tan i - \tan\eta_c \sin\beta_n}{\sin\varphi_n \sqrt{\cos^2(\varphi_n+\beta_n-\alpha_n)+\tan^2\eta_c \sin^2\beta_n}}\right)
\end{aligned} \tag{13}$$

In Eq. (13), η_c is the chip velocity angle. According to Stabler's rule [29], η_c is almost equal to the helix angle (i). β_n and ϕ_n are the friction and shear angles in the normal plane (P_n), respectively, and expressed by Eq. (14).

$$\tan\beta_n = \tan\beta \cos\eta_c, \quad \tan\varphi_n = \frac{r(\cos\eta_c/\cos i)\cos\alpha_n}{1 - r(\cos\eta_c/\cos i)\sin\alpha_n} \tag{14}$$

The shear angle (ϕ), shear stress (τ_s), friction coefficient (β) and chip thickness ratio (r) can be obtained by implementing the orthogonal cutting theory introduced in Ref. [13].

4. Effects of mesh dimension

4.1. *Chip morphology and cutting force results*

The orthogonal cutting simulations with local damage model were carried out to investigate the effect of mesh dimension on the chip morphology and cutting force. For the cutting condition $V = 300$ m/min and $t = 0.1$ mm, three different values of mesh dimension were established, namely meshx8, meshx12 and meshx16. These mesh dimensions were achieved by varying the number of elements in Y direction of the chip part (Wp-1). The mesh dimension for the separation layer (Wp-2) and workpiece support (Wp-3) was kept constant. The tool was meshed using 326 elements with 191 nodes. Table 4 presents the values of mesh dimensions.

The chip morphologies and cutting forces obtained from the high-speed cutting simulations with different mesh dimensions are presented in Figs. 4, and –6, where the equivalent plastic strain distributions can be observed.

In case of meshx8 (250 × 8 elements) with the coarse mesh dimension, the chip exhibited a continuous form, as given in Fig. 4a. The intensity of shear localization was not sufficient to form a segmented chip. This result was probably due to less plastic work done during the cutting process. When the mesh dimension was set to meshx12 (250 × 12 elements) with a finer mesh dimension, the chip was formed from both continuous and segmented parts, as seen in Fig 5a. Through the adjustment to meshx16 (250 × 16 elements) with the finest mesh dimension, adiabatic shear bands due to local strain localization occurred on the entire chip as can be observed in Fig. 6a, and this phenomenon caused the chip segmentation. That is, meshx16 with the finest mesh dimension allows the shear

Table 4
Mesh dimensions in the FE models.

Mesh dimension	Number of elements for workpiece			
(t = 0.1 mm)	Number of elements for chip	Characteristic element length for chip (mm)		
		X direction	Y direction	
meshx8	4750	250	8	0.00707
meshx12	5750	250	12	0.00577
meshx16	6750	250	16	0.005

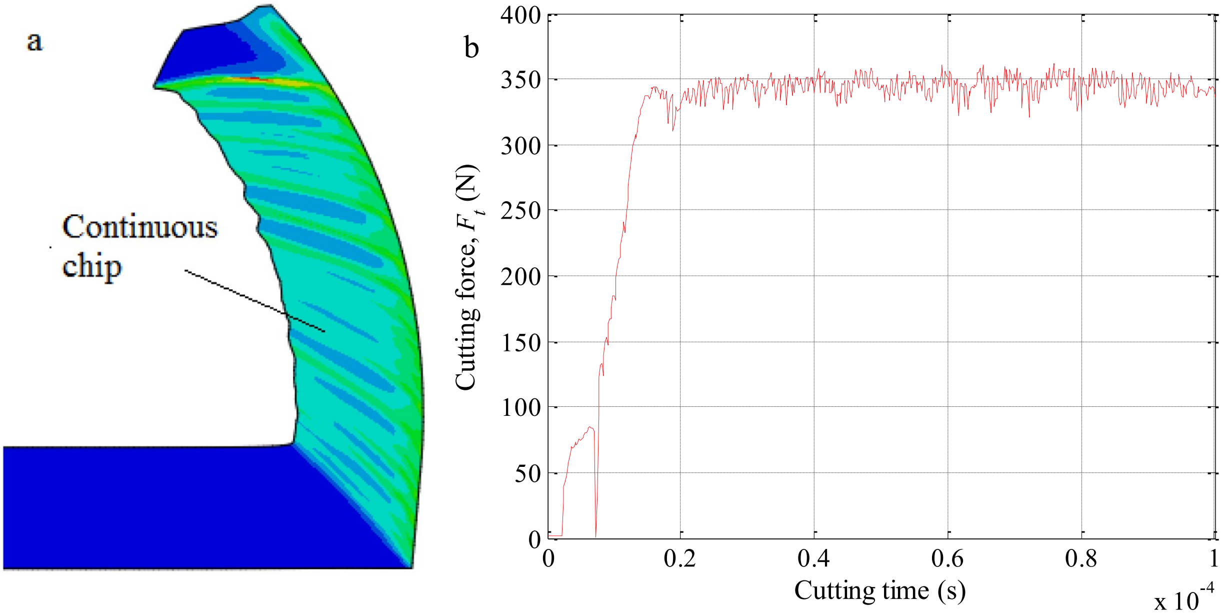

Fig. 4. The effect of mesh dimension for meshx8 (V = 300 m/min, t = 0.1 mm): (a) chip morphology; (b) tangential cutting force.

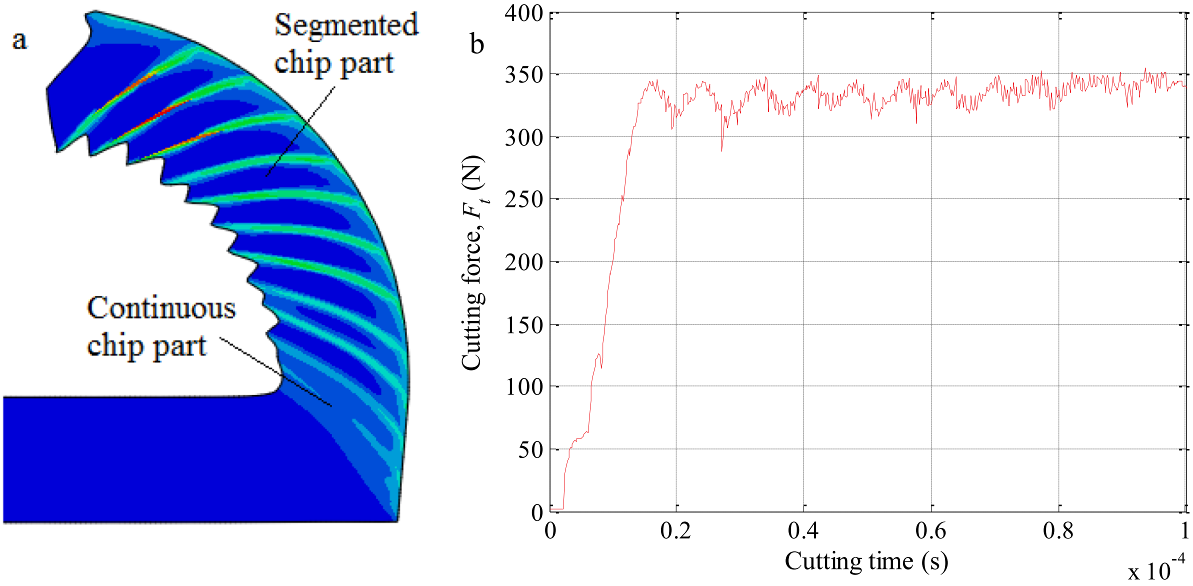

Fig. 5. The effect of mesh dimension for meshx12 (V = 300 m/min, t = 0.1 mm): (a) chip morphology; (b) tangential cutting force.

displacement. The local chip formation simulations indicate that the formation of shear bands is dependent on the mesh dimension. In other words, the strain gradient of elements varies with the mesh dimension, which results in the variation of chip morphology. To overcome the mesh dependency, the non-local damage model should be considered with the intrinsic material length [11].

The average tangential cutting force (F_t) was approximately 345 N for the simulation with the meshx8 (250 × 8 elements). Fig. 4b illustrates the variation of force F_t with cutting time. This coarse mesh which caused the continuous element removal resulted in the smooth variation of force F_t. The average force F_t from the meshx12 (250 × 12 elements) was found as 332 N. It was observed from Fig. 5b that the finer mesh generated both a periodic waved and flattened force curve (F_t). Through the finest elements with meshx16 (250 × 16 elements), the average force F_t was calculated as 326 N. As shown in Fig. 6b, the finest mesh leaded to increment in the force F_t before removing the element and instantaneous decrease when the element was completely removed. That is, there was a periodic fluctuation in the force F_t because of the chip segmentation. From the above discussion, it was deduced that the average tangential cutting forces computed from the FE models with three different mesh dimensions were nearly same although the force patterns were considerably dependent on the mesh dimension.

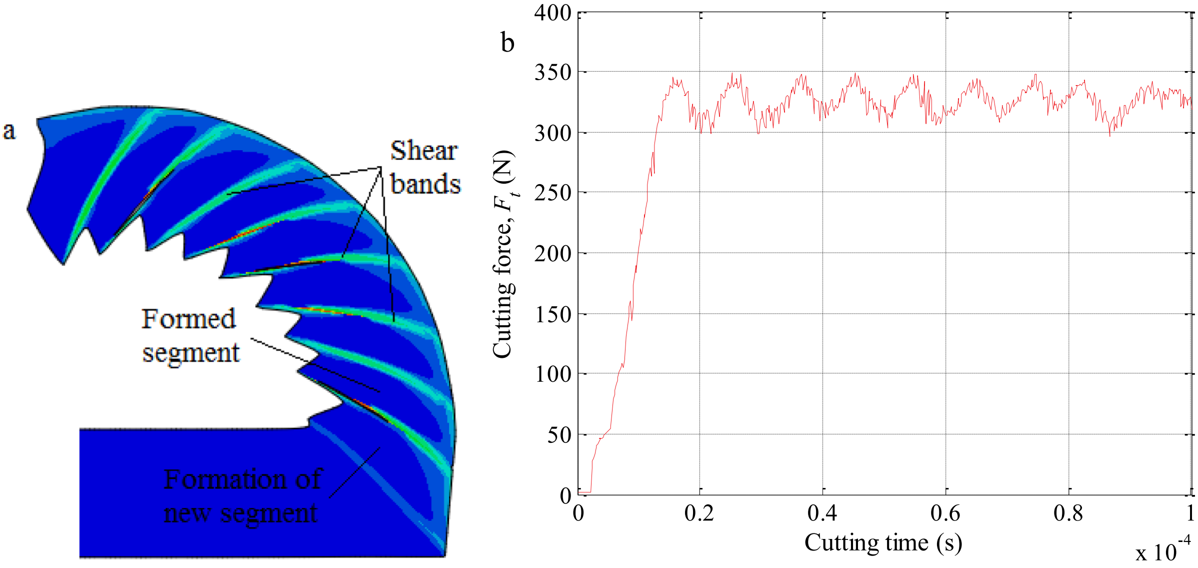

Fig. 6. The effect of mesh dimension for meshx16 (V = 300 m/min, t = 0.1 mm): (a) chip morphology; (b) tangential cutting force.

4.2. Application of intrinsic material length

The non-local damage model including the intrinsic material length was adopted to overcome the mesh dependency in cutting process simulations, and two different FE simulations with a failure plastic displacement ($\bar{u}_f^p$) were performed at the cutting condition V = 300 m/min and t = 0.3 mm. The time period of the simulations was 0.0003 s. The first simulation includes the characteristic length L = 0.015 mm (meshx16) applied to the chip part. Latter simulation was formulated with the characteristic length L = 0.01342 mm (meshx20) for the chip part. For these simulations, the thickness of the separation layer, 0.006 mm, was 50 times as small as the undeformed chip thickness, 0.3 mm. As observed in Fig. 7, the chip morphologies were approximately similar although the mesh densities were different. It can be deduced that the chip morphology is slightly sensitive to the mesh dimension because of energy dissipation having the constant plastic displacement. In the FE simulation with the characteristic length L = 0.015 mm, the calculation time was found as 24 min 23 s. When the FE model with the characteristic length L = 0.01342 mm was run, the cutting time reached to 40 min 6 s due to a finer mesh dimension (in a 2.6 GHz computer with 8GB RAM). In order to identify milling force constants, the meshx16 can be used in all the FE simulations.

Consequently, the numerical results were dependent on the mesh dimension when the local damage model was implemented. However, the non-local damage model significantly decreased the influence of mesh dimension.

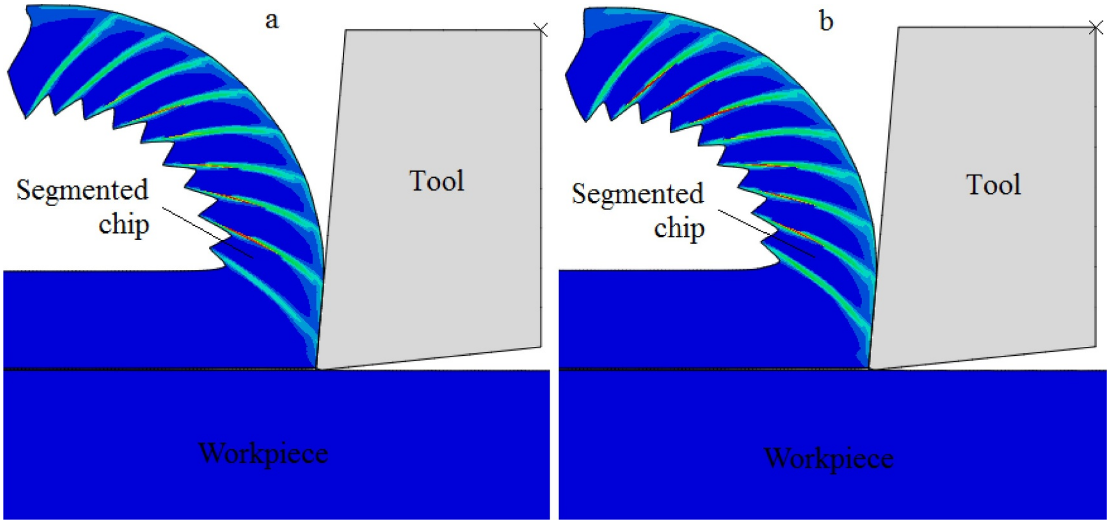

Fig. 7. The effect of mesh dimension on the chip morphology: (a) L = 0.015 mm; (b) L = 0.01342 mm.

4.3. Geometric characteristics of segmented chips

As shown in Fig. 8 which describes the segmented chip geometry obtained from the simulation run at the cutting condition $V = 300$ m/min and $t = 0.2$ mm, the shear bands were formed during high-speed cutting of Ti6Al4V. These deformations which generate the segmented chip cause chip thickness irregularity ranging from t_{min} to t_{max}. The segment ratio (S_r) and the segmentation frequency (f_{hz}) can be used to characterize the chip morphology.

The segment ratio can be defined by Eq. (15) [30].

$$S_r = \frac{t_{max} - t_{min}}{t_{max}} \tag{15}$$

Where t_{max} and t_{min} are the peak and valley section heights of the segmented chip, respectively.

The segmented chip consists of a series of trapezoids which arise from shearing planes. By considering the pitch of two neighbor shearing planes (d) and the chip sliding velocity (V_c), the segmentation frequency (f_{hz}) can be determined by Eq. (16) [31].

$$f_{hz} = \frac{V_c}{d} \tag{16}$$

Where the chip sliding velocity (V_c) is calculated using Eq. (17).

$$V_c = V\frac{\sin\varphi}{\cos(\varphi - \alpha_n)} \tag{17}$$

Fig. 9 shows the relationship between segment ratio (S_r) and undeformed chip thickness (t) based on Eq. (15). It was observed that with increasing the undeformed chip thickness, the segment ratio (S_r) became more obvious due to a transition occurrence from ductile to brittle fracture. This result indicates that the generated chips tend to become more segmented with increasing the undeformed chip thickness.

The variation of segmentation frequency (f_{hz}) at different undeformed chip thicknesses based on Eq. (16) is shown in Fig. 10. It was seen that the parameter f_{hz} decreased significantly with increasing the undeformed chip thickness. This is due to higher plastic deformation occurrence in the primary shear zone with increasing the undeformed chip thickness. Consequently, the geometrical characteristics of segmented chips can greatly help to understand the mechanism of chip formation.

4.4. Variation of tangential cutting force with undeformed chip thickness

The variations of the tangential cutting forces (F_t) with cutting time at the undeformed chip thicknesses $t = 0.2$ and 0.3 mm are illustrated in Fig. 11. It was seen that the fluctuation occurred because of the periodic formation of shear bands. The fluctuation frequencies of the force F_t correspond to those of chip segmentation. The average force F_t was 556 N with an amplitude of 105 N at the undeformed chip thickness $t = 0.2$ mm. In the case of the undeformed chip thickness $t = 0.3$ mm, the average force F_t was found as

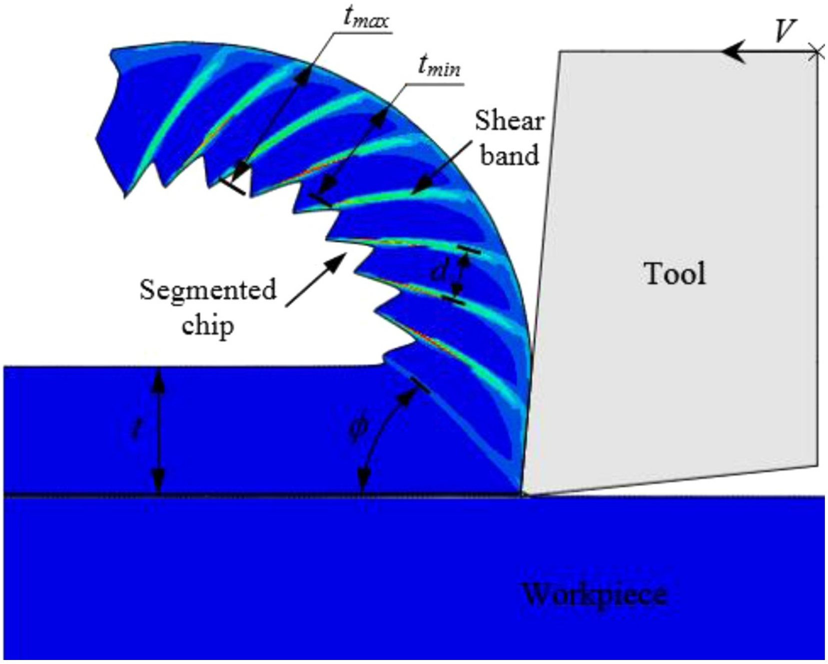

Fig. 8. Segmented chip morphology of Ti6Al4V simulated at $V = 300$ m/min and $t = 0.2$ mm.

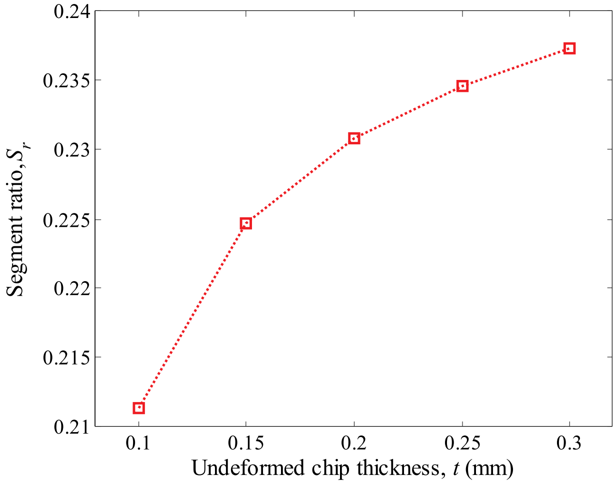

Fig. 9. Variation of segment ratio with undeformed chip thickness.

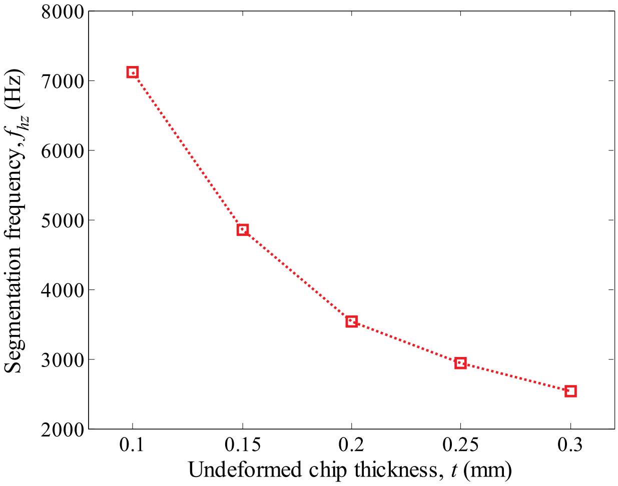

Fig. 10. Variation of segmentation frequency with undeformed chip thickness.

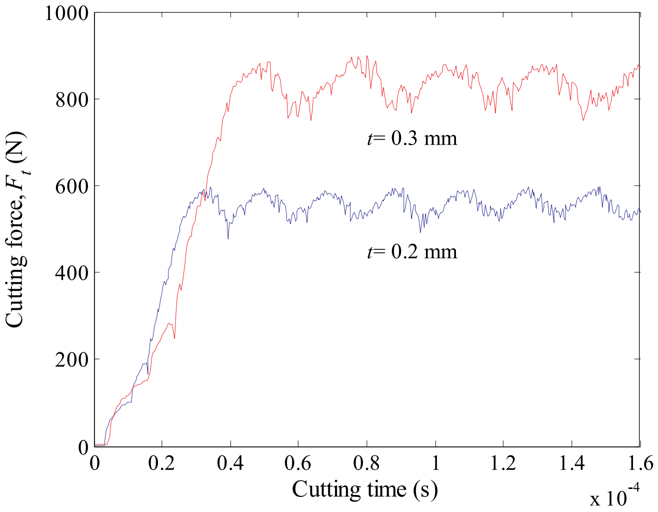

Fig. 11. Variations of tangential cutting forces with cutting time.

831 N with an amplitude of 162 N. Both the average and amplitude values of the force F_t at the undeformed chip thickness $t = 0.3$ mm were much greater than those at the undeformed chip thickness $t = 0.2$ mm.

The effect of the undeformed chip thicknesses on the average and amplitude values of the force F_t was also analyzed. Both the average and amplitude values of the force F_t linearly increased with increasing the undeformed chip thickness, as shown in Fig. 12. This increase leads to the higher local plastic deformation, and thus more plastic work is done in the primary deformation zone.

5. Milling force predictions

5.1. Edge and shear force constants

After analyzing the segmented chip formation at high cutting speed, the average values of tangential (F_t) and radial (F_r) cutting forces at each undeformed chip thickness were determined through the orthogonal cutting FE model based on the meshx16. The predicted forces F_t and F_r include the shear forces due to shearing at the shear zone and edge forces due to ploughing at the cutting edge for the particular tool-workpiece pair. The edge and shear force constants were established by applying the unified mechanics of cutting model [13] described in Section 3.2.

Fig. 13 shows the fitted curves between average cutting forces and undeformed chip thicknesses for tungsten carbide cutting tool and Ti6Al4V workpiece material. The least squares method was implemented to each curve, which provides the equations of the linear behavior and the correlation coefficients (R^2). The values of R^2 were close to 1, which show a good correlation. It was found that the forces F_t and F_r were linearly dependent on the undeformed chip thickness as follows:

$$\left.\begin{aligned} F_t &= 2569.9\,t + 51.185 \\ F_r &= 570.8\,t + 82.55 \end{aligned}\right\} \tag{18}$$

Comparing Eqs. (11) and (18), the edge force components F_{te} and F_{re} were found as 51.185 N and 82.55 N, respectively. In order to calculate the edge force constants K_{te} and K_{re}, these forces were divided by the cutting width.

In order to establish the shear force constants K_{ts}, K_{rs} and K_{as}, the basic cutting parameters, namely chip thickness ratio (r), shear angle (ϕ), shear stress (τ_s) and friction angle (β), were achieved by implementing the orthogonal cutting method. Besides, the edge force components F_{te} and F_{re} were subtracted from the predicted cutting forces F_t and F_r to determine the values of τ_s and β. Table 5 shows the basic cutting parameters derived through the FE simulations. It can be observed from the table that the results were slightly affected from the undeformed chip thickness. Therefore, the average values of the basic cutting parameters can be utilized for analyzing milling forces.

Substituting the values of τ_s and β into the oblique cutting model given by Eq. (13), the shear force constants K_{ts}, K_{rs} and K_{as} were identified. Table 6 represents the edge and shear force constants for Ti6Al4V workpiece machined using the tungsten carbide cutting tool with the normal rake angle of 5°. These empirical quantities were constant in the flat-end milling simulations since the helix angle (i) does not vary along the z direction. In the proposed approach, the cutting forces obtained from milling experiments would use as validation criterion. Hence, the accuracy of milling force constants was directly associated with the accuracy of the FE model.

5.2. Details of milling experiments

To validate the proposed predictive approach, three different milling cases have been considered: case 1 full immersion-slot milling – the entering angle (φ_{st}) is 0° and the leaving angle (φ_{ex}) is π, case 2 half immersion-up milling – φ_{st} is 0° and φ_{ex} is

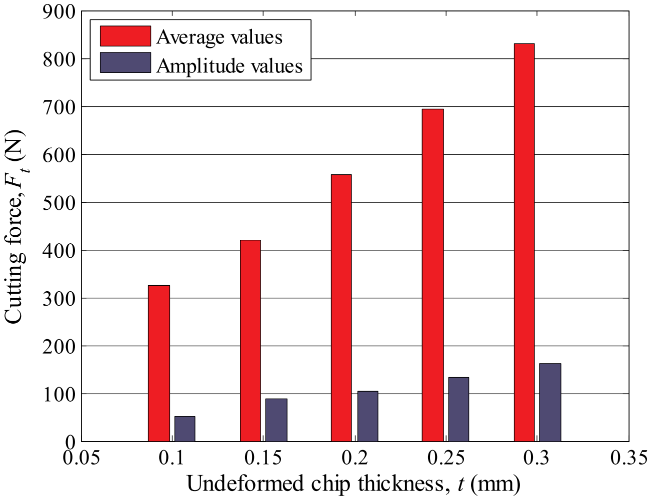

Fig. 12. Variation of tangential cutting forces with undeformed chip thickness.

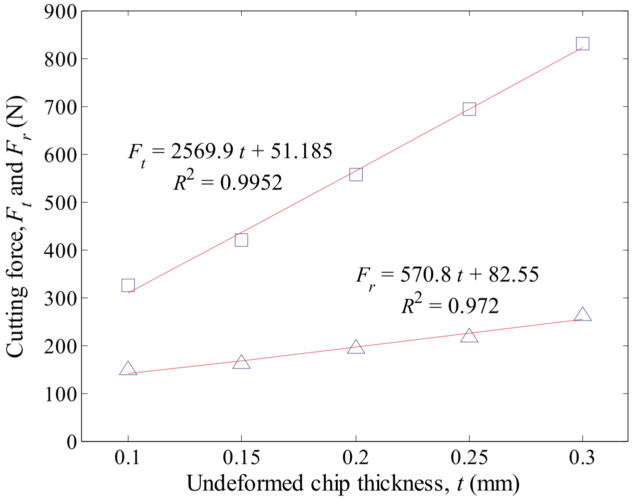

Fig. 13. The linearly fitted curves of the forces F_t and F_r.

Table 5
The basic cutting parameters.

Undeformed chip thickness, t (mm) β (°) τ_s (MPa)	Chip thickness ratio, r Shear stress,	Shear angle, ϕ (°)	Friction angle,	
0.10	0.9243	45.0	24.5	484.4
0.15	0.9598	46.2	21.9	446.8
0.20	0.9733	46.7	21.1	459.5
0.25	0.9791	46.8	19.8	478.3
0.30	0.9722	46.6	20.3	476.0
Average	0.9617	46.3	21.5	469.0

Table 6
The edge and shear force constants.

α_n (°)	K_{ts} (N/mm^2)	K_{te} (N/mm)	K_{rs} (N/mm^2)	K_{re} (N/mm)	K_{as} (N/mm^2)	K_{ae} (N/mm)
5	1330.9	25.6	357.8	41.3	460.9	0

described as π/2 and case 3 half immersion-down milling − φ_{st} is π/2 and φ_{ex} is π. In each case, two different feeds per tooth f_t = 0.025 and 0.05 mm/tooth were studied while the cutting speed (V) and the cutting depth (a_p) were set to 300 m/min and 1 mm, respectively. The experimental set-up can be seen in Fig. 14.

The high-speed milling experiments were conducted on a Quaser MV154C machining center. A two-fluted carbide flat-end mill having a diameter of 12 mm and helix angle of 30° was used to machine the Ti6Al4V workpiece. The measurements were performed using Kistler 9257B dynamometer connected to Kistler 5070A charge amplifier. The force signals were collected using a sampling rate of 7957 Hz. The post processing of the force signals was carried out with Dyanoware software.

5.3. Analysis of milling forces and validation

For analyzing the performance of the proposed predictive approach, the simulated forces have been compared with the measured forces as shown in Figs. 15, and –17. The absolute deviation percentages between the simulated and measured average forces were specified to evaluate the accuracy of milling force predictions.

Fig. 15 shows the predicted and measured instantaneous force components F_x, F_y and F_z at the feed rate f_t = 0.025 mm/tooth and cutting speed V = 300 m/min for a full immersion-slot milling. The measured forces exhibited slightly varying amplitudes whereas the predicted ones showed unique amplitudes. The milling force model with the force constants established numerically from the FE model introduced a deviation percentage of 5.6 for F_x and 2.69 for F_y. However, the deviation percentage for F_z was high up to 17.4. Under the cutting condition with higher feed per toothf_t = 0.05 mm/tooth, the deviation percentages were calculated as 5.84, 10.21 and 19.88 for F_x, F_y and F_z, respectively. These results reveal that the relatively low forces, especially force F_z, can be affected from the noise during force measurements.

Under the feed rate f_t = 0.025 mm/tooth and cutting speed V = 300 m/min for a half immersion-up milling, Fig. 16 shows the variations of the predicted and measured instantaneous force components F_x, F_y and F_z with the rotation angle. The predicted forces

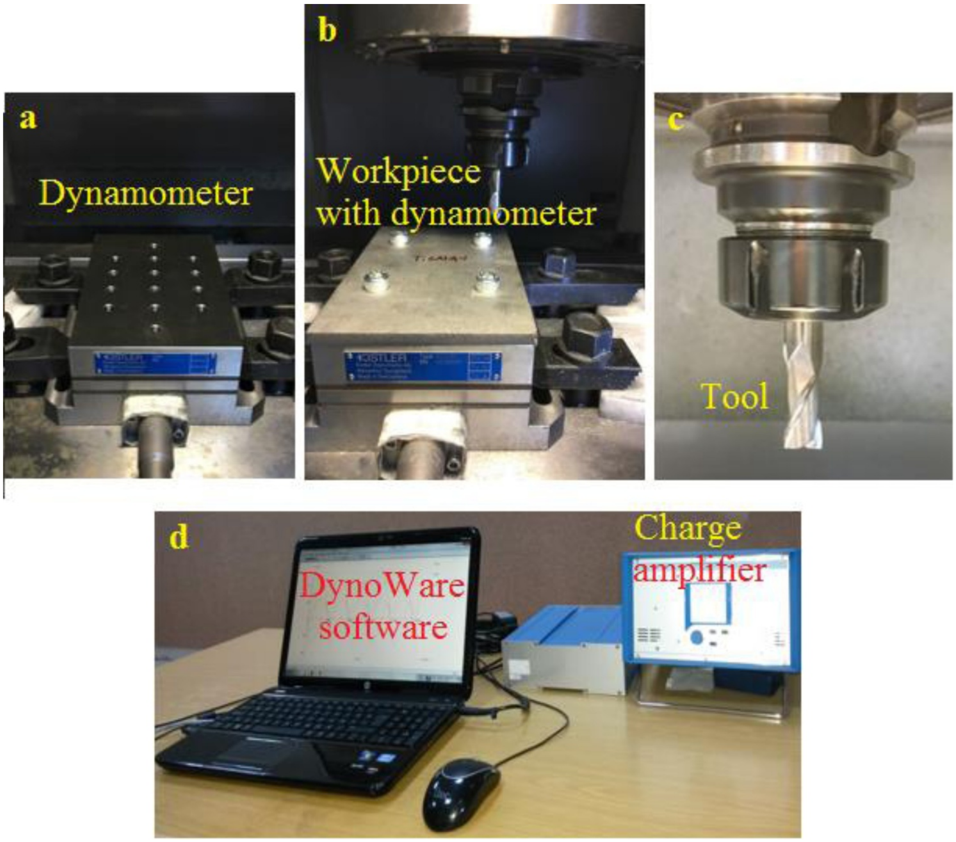

Fig. 14. Experimental set-up: (a) dynamometer; (b) workpiece on dynamometer; (c) end mill tool; (d) charge amplifier and dynoware software.

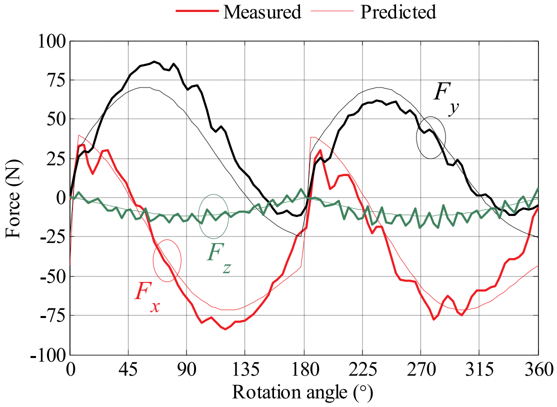

Fig. 15. Experimental validation of F_x, F_y and F_z at $f_t = 0.025$ mm/tooth and $V = 300$ m/min for slot milling.

F_x and F_y properly matched with the measured ones in pattern. There was a clear difference in the peak values for F_z. This appears probably due to the tool-workpiece vibrations during cutting operation. The milling force model with the force constants identified following the FE method produced a relatively low deviation percentage of 15.92 in the calculation of the force F_x. The deviation percentages for F_y and F_z were also 7.33 and 5.99, respectively. The deviations between the simulated and measured cutting forces may because the milling force model deals with the only peripheral cutting edges of flat-end mill tool. When the feed rate (f_t) was increased to 0.05 mm/tooth under the same cutting speed, the deviation percentages were high up to 20.51 for F_x and 18.27 for F_y. However, the absolute deviation was found as less than 10% for F_z. It was evident that the prediction accuracies of milling forces were affected from the increase in feed per tooth.

As seen in Fig. 17, the patterns F_x and F_y which were determined from the force constants established by using the FE model did not exactly fit to those obtained experimentally at the feed rate $f_t = 0.025$ mm/tooth and cutting speed $V = 300$ m/min for a half immersion-down milling. For modeling the variations in the peaks, the tool runout is studied as shown in Ref. [32]. The proposed

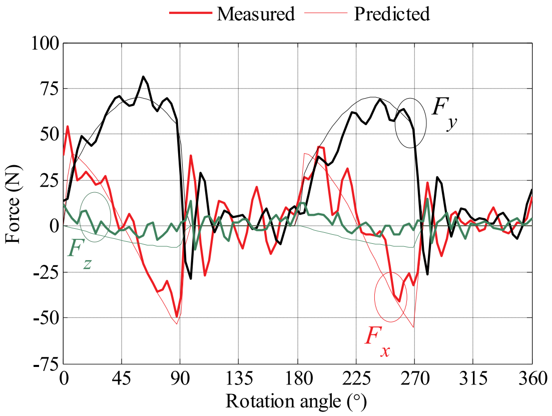

Fig. 16. Experimental validation of F_x, F_y and F_z at f_t = 0.025 mm/tooth and V = 300 m/min for up milling.

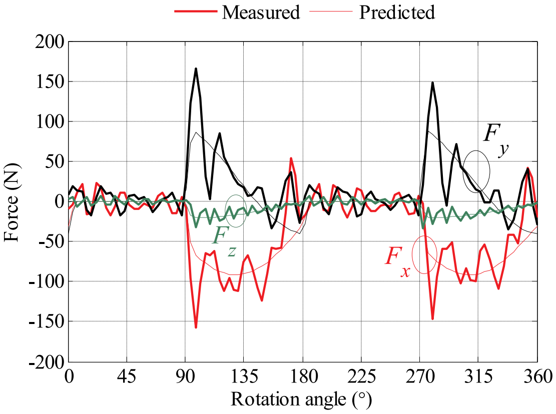

Fig. 17. Experimental validation of F_x, F_y and F_z at f_t = 0.05 mm/tooth and V = 300 m/min for down milling.

approach deals with the milling force model which does not include the tool runout. On the other hand, the average forces F_x, F_y and F_z predicted from the analytical simulations were close to those of the experimental tests with a deviation of about 10%. In analyzing the case of the higher feed rate f_t = 0.05 mm/tooth, the deviation percentages were found as 13.14, 14.2 and 15.15 for F_x, F_y and F_z, respectively. That is, their prediction accuracies were about 85%. It can be inferred that the use of numerically obtained force constants provides a satisfactory prediction of milling forces.

6. Conclusions

In this paper, a simplified and efficient process simulation approach has been proposed for the prediction of cutting forces in high-speed flat-end milling of Ti6Al4V alloy. This approach composes of two main parts: FE modeling of segmented chip formation and modeling of milling forces. The first contribution of this approach was that a FE model of the orthogonal cutting was developed to analyze the segmented chip formation. In the simulations of segmented chip formation, the effect of mesh dimension was systematically studied by applying a displacement-based ductile failure criterion. The numerical results indicated that the average tangential cutting force was slightly affected from the mesh dimension. In the simulation with the local damage model having a coarse mesh, the continuous chip was achieved because of inadequate shear deformation. Through a finer mesh, the higher shear localization occurred and the segmentation of the chips increased. Besides, the chips tended to be become more segmented due to the transition from ductile to brittle fracture as the undeformed chip thickness increased. In the non-local damage models which were established with different characteristic lengths involving a failure plastic displacement, the chip morphology became independent from the mesh dimension. Its other contribution was to predict the cutting forces in high-speed flat-end milling by using the unified mechanics of cutting approach and the numerical FE simulation instead of experimental tests for the determination of milling force constants. It was shown by comparing predictions with measurement results that the flat-end milling forces can be accurately produced by modeling the chip formation process through the FE model based on the JC material and failure laws. All the information required for predicting milling forces is tool geometry and workpiece material properties. The proposed approach can be applied as an alternative tool for providing higher productivity and a significant reduction in manufacturing cost.

Supplementary materials

Supplementary material associated with this article can be found, in the online version, at doi:10.1016/j.simpat.2019.102039.

References

[1] J.D.P. Velásquez, B. Bolle, P. Chevrier, G. Geandier, A. Tidu, Metallurgical study on chips obtained by high speed machining of a Ti–6 wt%Al–4 wt%V alloy, Mater. Sci. Eng. A 452–453 (2007) 469–474.
[2] M. Bäker, J. Rösler, C. Siemers, The influence of thermal conductivity on segmented chip formation, Comput. Mater. Sci 26 (2003) 175–182.
[3] C. Hortig, B. Svendsen, Simulation of chip formation during high-speed cutting, J. Mater. Process. Technol. 186 (2007) 66–76.
[4] Y. Zhang, T. Mabrouki, D. Nelias, Y. Gong, FE-model for titanium alloy (Ti-6Al-4 V) cutting based on the identification of limiting shear stress at tool-chip interface, Int. J. Mater. Form 4 (2011) 11–23.
[5] A. Shams, M. Mashayekhi, Improvement of orthogonal cutting simulation with a nonlocal damage model, Int. J. Mech. Sci. 61 (2012) 88–96.
[6] G.R. Johnson, W.H. Cook, A constitutive model and data for metals subjected to large strains, high strain rates and high temperatures, Proceedings of the 7th International Symposium on Ballistics, The Hague, The Netherlands, 1983, pp. 541–547.
[7] R.J. Saffar, M.R. Razfar, O. Zarei, E. Ghassemieh, Simulation of three-dimension cutting force and tool deflection in the end milling operation based on finite element method, Simul. Model. Pract. Theory 16 (2008) 1677–1688.
[8] M. Aydin, Prediction of cutting speed interval of diamond-coated tools with residual stress, Mater. Manuf. Process. 32 (2017) 145–150.
[9] A. Qasim, S. Nisar, A. Shah, M.S. Khalid, M.A. Sheikh, Optimization of process parameters for machining of AISI-1045 steel using Taguchi design and Anova, Simul. Model. Pract. Theory 59 (2015) 36–51.
[10] B. Wang, Z. Liu, Shear localization sensitivity analysis for Johnson–Cook constitutive parameters on serrated chips in high speed machining of Ti6Al4V, Simul. Model. Pract. Th. 55 (2015) 63–76.
[11] R. Ambati, H. Yuan, FEM mesh-dependence in cutting process simulations, Int. J. Adv. Manuf. Tech. 53 (2011) 313–323.
[12] G. Chen, C. Ren, X. Yang, X. Jin, T. Guo, Finite element simulation of high-speed machining of titanium alloy (Ti–6Al–4V) based on ductile failure model, Int. J. Adv. Manuf. Technol. 75 (2014) 1065–1076.
[13] E. Budak, Y. Altintas, E.J.A. Armarego, Prediction of milling force coefficients from orthogonal cutting data, Trans. ASME J. Manuf. Sci. Eng. 118 (1996) 216–224.
[14] S. Rao, M.S. Shunmugam, Analytical modeling of micro end-milling forces with edge radius and material strengthening effects, Mach. Sci. Technol. 16 (2012) 205–227.
[15] M. Wan, W.J. Pan, W.H. Zhang, Y.C. Ma, Y. Yang, A unified instantaneous cutting force model for flat end mills with variable geometries, J. Mater. Process. Technol. 214 (2014) 641–650.
[16] M.K. Dikshit, A.B. Puri, A. Maity, Analysis of cutting force coefficients in high-speed ball end milling at varying rotational speeds, Mach. Sci. Technol. 21 (2017) 416–435.
[17] M. Aydın, M. Uçar, A. Cengiz, M. Kurt, Identification of static surface form errors from cutting force distribution in flat-end milling processes, J. Braz. Soc. Mech. Sci. 37 (2015) 1001–1013.
[18] O.B. Adetoro, P.H. Wen, Prediction of mechanistic cutting force coefficients using ALE formulation, Int. J. Adv. Manuf. Technol. 46 (2010) 79–90.
[19] O. Gonzalo, H. Jauregi, G. Uriarte, L.N. Lopez de Lacalle, Prediction of specific force coefficients from a FEM cutting model, Int. J. Adv. Manuf. Technol. 43 (2009) 348–356.
[20] M. Aydın, U. Köklü, Identification and modeling of cutting forces in ball-end milling based on two different finite element models with arbitrary Lagrangian Eulerian technique, Int. J. Adv. Manuf. Technol. 92 (2017) 1465–1480.
[21] B. Wang, Z. Liu, Investigations on the chip formation mechanism and shear localization sensitivity of high-speed machining Ti6Al4V, Int. J. Adv. Manuf. Technol. 75 (2014) 1065–1076.
[22] M. Bäker, Finite element simulation of high-speed cutting forces, J. Mater. Process. Technol. 176 (2006) 117–126.
[23] M. Bäker, Finite element investigation of the flow stress dependence of chip formation, J. Mater. Process. Technol. 167 (2005) 1–13.
[24] G.R. Johnson, T.J. Holmquist, Test data and computational strength and fracture model constants for 23 materials subjected to large strains, high strain rates, and high temperatures, LA-11463-MS, Los Alamos National Laboratory, (1989).
[25] F.K. Chang, K.Y. Chang, A progressive damage model for laminated composites containing stress concentrations, J. Compos. Mater. 21 (1987) 834–855.
[26] G.R. Johnson, W.H. Cook, Fracture characteristics of three metals subjected to various strains, strain rates, temperatures and pressures, Eng. Fract. Mech. 21 (1985) 31–48.
[27] W.A. Kline, R.E. DeVor, I.A. Shareef, The prediction of surface accuracy in end milling, Trans. ASME J. Eng. Ind. 104 (1982) 272–278.
[28] E.J.A. Armarego, R.C. Whitfield, Computer based modeling of popular machining operations for force and power prediction, CIRP Ann. Manuf. Technol. 34 (1985) 45–49.
[29] G.V. Stabler, Fundamental geometry of cutting tools, Proc. Inst. Mech. Eng. 165 (1951) 14–26.
[30] H. Schulz, E. Abele, A. Sahm, Material aspects of chip formation in HSC machining, CIRP Ann. Manuf. Technnol. 50 (2001) 45–48.
[31] S. Joshi, A. Tewari, S.S. Joshi, Microstructural characterization of chip segmentation under different machining environments in orthogonal machining of Ti6Al4V, J. Eng. Mater. Technol. 137 (2015) 011005.
[32] M. Wan, W.H. Zhang, G.H. Qin, G. Tan, Efficient calibration of instantaneous cutting force coefficients and runout parameters for general end mills, Int. J. Mach. Tools Manuf. 47 (2007) 1767–1776.